RSC Advances

PAPER

View Article Online
View Journal | View Issue

Cite this: *RSC Adv.*, 2019, **9**, 8065

Ag_3PO_4 nanocrystals and g-C_3N_4 quantum dots decorated Ag_2WO_4 nanorods: ternary nanoheterostructures for photocatalytic degradation of organic contaminants in water†

Chang Liu,[a] Jingbo Wang,[b] Shuang Yang,[b] Xiuying Li*[a] and Xue Lin*[b]

Received 29th November 2018
Accepted 27th February 2019

DOI: 10.1039/c8ra09815h

rsc.li/rsc-advances

Visible-light-driven Ag_3PO_4/graphite-like carbon nitride/Ag_2WO_4 photocatalysts with different weight fractions of Ag_3PO_4 were synthesized. Ag_2WO_4 nanorods with a scale of 500 nm to 3 μm were prepared by using a hydrothermal reaction. *Via* a facile deposition–precipitation technique, graphite-like carbon nitride (g-C_3N_4) quantum dots and Ag_3PO_4 nanocrystals were then deposited onto the surface of Ag_2WO_4 nanorods sequentially. Under visible-light irradiation (λ > 420 nm), the Ag_3PO_4/g-C_3N_4/Ag_2WO_4 nanorods degraded Rh B efficiently and displayed much higher photocatalytic activity than that of pure Ag_2WO_4 and the g-C_3N_4/Ag_2WO_4 composite, and the Ag_3PO_4/g-C_3N_4/Ag_2WO_4 hybrid photocatalyst with 30 wt% of Ag_3PO_4 exhibited the highest photocatalytic activity. The quenching effects of different scavengers demonstrated that reactive h^+ and $\cdot O^{2-}$ played the major roles in Rh B degradation. It was elucidated that the excellent photocatalytic activity of Ag_3PO_4/g-C_3N_4/Ag_2WO_4 for the degradation of Rh B under visible light (λ > 420 nm) can be ascribed to the efficient separation of photogenerated electrons and holes through the Ag_3PO_4/g-C_3N_4/Ag_2WO_4 heterostructure.

1. Introduction

The development of visible-light-driven photocatalysts with excellent performance and good stability is a precondition for harvesting more sunlight and realizing efficient photocatalysis. In recent years, Ag-based photocatalysts, such as AgX (where X = Cl, Br, and I), Ag_2O, Ag_2CO_3, $Ag_6Si_2O_7$, Ag_2WO_4, Ag_3PO_4, and $Ag_2Mo_2O_7$, have been developed for photocatalysis applications.[1–8] Among those Ag-based photocatalysts, Ag_2WO_4 has been the most studied because of its weak crystal field and was verified to exhibit H_2 evolution and organic pollution degradation ability under UV light irradiation.[9] However, the band gap of Ag_2WO_4 is theoretically calculated to be 3.55 eV, resulting in its sluggish reaction to visible light, like TiO_2.[10] Thereupon, many efforts have been devoted to make Ag_2WO_4 sensitive to visible light, including its combination with sensitizers, *i.e.*, AgI, Ag/AgCl, and Ag. Unfortunately, Ag_2WO_4 itself has not yet been modified to be sensitive to visible light.[11–13] However, some researchers found that Ag_3PO_4 shows strong oxidation power, which can achieve quantum efficiency of up to 90% under visible light for O_2 generation from water splitting.[14,15] However, as Ag_3PO_4 is light-sensitive and slightly soluble in aqueous solution, it will be photocorroded and decompose to weakly active Ag during the photodegradation, and, accordingly, the photocatalytic activity gradually deteriorates, which is the main hindrance for the practical application of Ag_3PO_4 as a recyclable and highly efficient photocatalyst. Recent reports have shown that forming complexes with special structures such as core–shell nanostructures, plasmonic structures, and heterostructures could not only effectively protect the Ag_3PO_4 crystals from dissolution in aqueous solutions but also enhance their stabilities and photocatalytic performance.[15,16] Therefore, modifying Ag_2WO_4 with Ag_3PO_4 could significantly accelerate the transfer of photogenerated charge carriers.

Nowadays, graphite-like carbon nitride (g-C_3N_4) has been studied as a promising candidate for hydrogen evolution and environment purification under visible-light irradiation.[17–19] Although g-C_3N_4 possesses good chemical and thermal stability, its use in photocatalysis is limited because of its high recombination of photogenerated electron–hole pairs.[20] To solve this problem, abundant strategies, including doping, deposition, and sensitization, were developed.[20–23] Constructing the heterostructure is also an effective approach for decreasing the recombination rate of photogenerated charges. However, most of the reported g-C_3N_4 nanostructures are composed of stacked two-dimensional nanosheets, and very few available examples concentrating on zero-dimensional quantum dots (QDs) exist, especially on QD-based heterostructures.[19,24] Given the

[a]*Key Laboratory of Preparation and Application of Environmental Friendly Materials, Jilin Normal University, Ministry of Education, Changchun 130103, China*
[b]*College of Material Science and Engineering, Beihua University, Jilin 132013, China. E-mail: jlsdlinxue@126.com; Fax: +86 434 329 2154; Tel: +86 1569434 9717*

† Electronic supplementary information (ESI) available. See DOI: 10.1039/c8ra09815h

enhanced light absorption and, more importantly, excellent electron conductivity of carbon materials, it is rationally speculated that decoration of Ag_2WO_4 with g-C_3N_4 QDs in an intimate integration fashion would significantly improve the photocatalytic performances of Ag_2WO_4.

Herein, we report a successful attempt at the preparation of Ag_3PO_4/g-C_3N_4/Ag_2WO_4 nanoheterostructures *via* a facile *in situ* precipitation synthetic strategy. The photocatalytic performance of the ternary composite was investigated by measuring the photodegradation of rhodamine B (Rh B) under visible-light irradiation ($\lambda > 420$ nm). Up to date, construction of Ag_3PO_4/g-C_3N_4/Ag_2WO_4 ternary heterostructures in combination with a systematic study on the photocatalysis mechanism has not yet been reported.

2. Experimental

2.1 Preparation of photocatalysts

2.1.1 Preparation of Ag_2WO_4 nanorods. All reagents for synthesis and analysis were commercially available and used without further treatments. The Ag_2WO_4 nanorods were synthesized through a facile hydrothermal method. In a typical procedure, a solution of Na_2WO_4 (0.10 mol L^{-1}, 10 mL H_2O) was stirred for 30 min, then 20 mL aqueous solution of $AgNO_3$ (0.40 mol L^{-1}, 5 mL H_2O) was dropped slowly into the above solution, which was stirred magnetically for another 30 min. The mixed solution was transferred into a 20 mL Teflon-lined steel autoclave, which was heated in an oven at 160 °C for 24 h. Then the system was allowed to cool to room temperature naturally. Lastly, the obtained samples were collected and washed with ethanol and distilled water several times then and dried at 70 °C for 2 h.

2.1.2 Preparation of g-C_3N_4 QDs. Bulk g-C_3N_4 was prepared by heating melamine for 4 h to 550 °C and keeping it at this temperature for another 4 h in air.[24] g-C_3N_4 QDs was prepared by using Yu's method:[24] First, 1 g of bulk g-C_3N_4 was treated in the mixture of concentrated sulfuric acid (H_2SO_4) (20 mL) and nitric acid (HNO_3) (20 mL) for ~2 h at room temperature. The mixture was then diluted with deionized water (1 L) and washed several times. Second, 50 mg of the obtained solid was dispersed in 30 mL concentrated $NH_3 \cdot H_2O$, and then the mixed suspension was transferred into a 20 mL Teflon-lined stainless-steel autoclave and heated at 200 °C for 24 h. Upon cooling to room temperature, the precipitate was washed with water several times to remove the adsorbed NH_3 molecules. Third, 10 mg of the synthesized solid was dispersed in 100 mL of water, and then treated ultrasonically for ~6 h. The as-obtained aqueous suspension was then centrifuged at ~7000 rpm and dialyzed in a dialysis bag to remove large-sized nanoparticles.

2.1.3 Preparation of g-C_3N_4/Ag_2WO_4 photocatalyst. The as-prepared Ag_2WO_4 nanorods (300 mg) were mixed with 200 mL of deionized water by ultrasonication for 30 min. Then, 1.0 mL of a 5% polyethylene glycol (PEG) 2000 solution was added and the dispersion was stirred for another 10 min. For wrapping g-C_3N_4 QDs on Ag_2WO_4 nanorods, 30 mL of the g-C_3N_4 QDs solution (1 mg mL^{-1}) was added and the reaction temperature was kept at 70 °C for 60 min. The resulting suspension was filtered, washed with deionized water three times, and dried at 60 °C for 24 h in a vacuum oven. The theoretical wrapping amount of g-C_3N_4 QDs was 10 wt%.

2.1.4 Preparation of Ag_3PO_4/g-C_3N_4/Ag_2WO_4 photocatalyst. The Ag_3PO_4/g-C_3N_4/Ag_2WO_4 hybrid photocatalyst was synthesized through an *in situ* precipitation method at room temperature. In a typical process, g-C_3N_4/Ag_2WO_4 nanorods (300 mg) were dispersed in 100 mL of deionized water by ultrasound for 30 min, and then an emulsion of $AgNO_3$ + Na_2HPO_4 (with a molar ratio of Ag : P = 3 : 1) was dropwise added to the suspension under magnetic stirring. The pH value was adjusted to 3 by adding 1.0 M NaOH. The resulting suspension was stirred in the dark for another 30 min. Finally, the precipitate was washed with deionized water three times, collected by centrifugation, and then dried at 60 °C in the vacuum drying oven to obtain Ag_3PO_4/g-C_3N_4/Ag_2WO_4 (denoted as 10% Ag_3PO_4/g-C_3N_4/Ag_2WO_4, 20% Ag_3PO_4/g-C_3N_4/Ag_2WO_4, 30% Ag_3PO_4/g-C_3N_4/Ag_2WO_4, 40% Ag_3PO_4/g-C_3N_4/Ag_2WO_4, and 50% Ag_3PO_4/g-C_3N_4/Ag_2WO_4, respectively).

2.2 Characterization of photocatalysts

X-ray diffraction (XRD) was performed on a D/MAX 2500 V diffractometer (Rigaku, Japan) with monochromatized Cu K_α radiation, $\lambda = 0.15418$ nm, and the scanning range was from 10° to 70°. The morphologies and microstructures of the products were characterized by transmission electron microscopy (TEM, JEM-2100F). X-ray photoelectron spectroscopy (XPS, VG Scientific) using 300 W Al K_α radiation as the excitation source was applied to study the composition and chemical state of the elements. Fourier-transform infrared spectroscopy (FT-IR) spectra were obtained with an FT-IR spectrometer (America Perkin Elmer, Spectrum One) using the standard KBr disk method. UV-vis diffuse reflection spectra (DRS) of the samples were tested on a scan UV-vis spectrophotometer (UV-2550) equipped with an integrating sphere using $BaSO_4$ as the reference sample. The surface areas were measured by using the nitrogen adsorption Brunauer–Emmett–Teller (BET) method (BET/BJH Surface Area, 3H-2000PS1).

2.3 Photocatalytic activities study

The photocatalytic properties of the as-prepared samples were evaluated using Rh B as a model compound. In experiments, the Rh B solution (0.01 mmol L^{-1}, 100 mL) containing 0.02 g of photocatalyst were mixed in a Pyrex reaction glass. The reactivity experiments were conducted in air at room temperature. A 300 W Xe lamp ($\lambda > 420$ nm) with 100 mW cm^{-2} illumination intensity was employed to provide visible-light irradiation. A 420 nm cutoff filter was inserted between the lamp and the sample to filter out UV light ($\lambda < 420$ nm). Prior to visible-light illumination, the suspension was strongly stirred in the dark for 40 min. Then the solution was exposed to visible-light irradiation under magnetic stirring. At given time intervals, 4 mL of the suspension was periodically collected and analyzed after centrifugation. The Rh B concentration was analyzed by using a UV-2550 spectrometer to record the intensity of the maximum band at 552 nm in the UV-vis absorption spectra.

2.4 Active species trapping experiments

For detecting the active species during photocatalytic reactivity, some sacrificial agents, such as 2-propanol (IPA), disodium ethylenediamine tetraacetic acid (EDTA-2Na), and 1,4-benzoquinone (BQ) were used as the hydroxyl radical ($\cdot$OH) scavenger, hole (h^+) scavenger, and superoxide radical ($O_2^{\bullet -}$) scavenger, respectively. The method was similar to the former photocatalytic activity test with the addition of 1 mmol of quencher in the presence of Rh B.

3. Results and discussion

To determine the crystal form of as-prepared samples, the XRD patterns were recorded, as shown in Fig. 1. Pure Ag_2WO_4 shows obvious diffraction peaks at $2\theta = 30.2°$, 31.4°, 33.0°, and 45.4°, which are attributed to the (002), (231), (400), and (402) diffraction planes of α-Ag_2WO_4 (JCPDS no. 34-0061), respectively.[25] For the pure g-C_3N_4 sample, the diffraction peak at 27.4° can be clearly observed, which are indexed to (002) plane of g-C_3N_4.[26] From the XRD pattern of the g-C_3N_4/Ag_2WO_4 composite, all the crystal planes of α-Ag_2WO_4 can be detected. However, there are no any diffraction peaks of g-C_3N_4 that can be observed for the g-C_3N_4/Ag_2WO_4 sample, owing to small crystal size of g-C_3N_4 QDs.[26] For the pure Ag_3PO_4, the diffraction peaks can be indexed to the cubic structure of Ag_3PO_4 (JCPDS 06-0505). The diffraction peaks of Ag_3PO_4 are clearly observed in Ag_3PO_4/g-C_3N_4/Ag_2WO_4 composites, and the intensities of the diffraction peaks of Ag_3PO_4 increase with increasing weight ratio of Ag_3PO_4 in the composites.

Herein, the successful loading of g-C_3N_4 QDs was illustrated by FT-IR spectra, as displayed in Fig. 2. The main characteristic peaks of g-C_3N_4 QDs are observed in both g-C_3N_4/Ag_2WO_4 and Ag_3PO_4/g-C_3N_4/Ag_2WO_4 spectra, showing the successful loading of g-C_3N_4 QDs. The absorption bands at 1700–800 cm^{-1} are attributed to either C=N or C–N stretching vibrations.[19] The broad range centered at 3200 cm^{-1} can be ascribed to the N–H stretching vibration.[19]

XPS measurement was also employed to investigate the surface chemical states of the Ag_3PO_4/g-C_3N_4/Ag_2WO_4 composite. Fig. 3a shows the XPS spectrum of Ag 3d; two

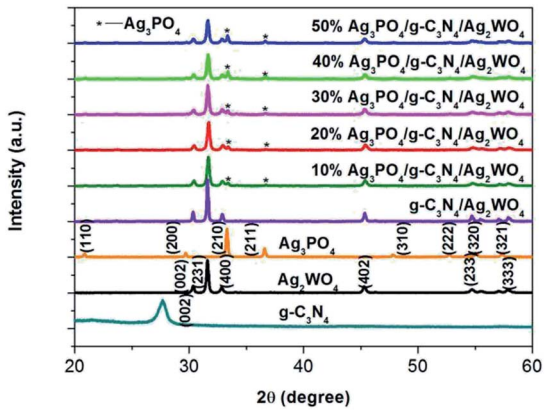

Fig. 1 XRD patterns of the as-prepared samples.

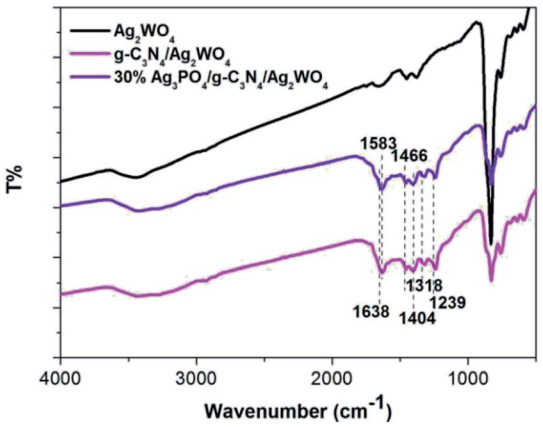

Fig. 2 FT-IR spectra of the as-prepared samples.

different peaks centered at binding energies of 366.5 and 372.6 eV can be detected, and these are assigned to Ag $3d_{5/2}$ and Ag $3d_{3/2}$,[27] respectively. The XPS spectrum of W 4f shows two different peaks centered at 38.3 and 36.1 eV, which are ascribed to W $4f_{5/2}$ and W $4f_{7/2}$, respectively (Fig. 3b).[26] The P 2p peak is observed at ~134.1 eV (Fig. 3c), corresponding to P^{5+}.[27] As can be seen in the XPS spectrum of C 1s (Fig. 3d), the peak at 283.3 eV can be assigned to the sp^2-bonded carbon in C–C, whereas the peak located at 287.0 eV reveals the formation of N–C=N.[19] The XPS spectrum of N 1s can be deconvoluted into two peaks with binding energies at 397.5 and 400.0 eV, which are attributed to C–N=C and $(N–(C)_3)$,[19] respectively.

Fig. 4 shows scanning electron microscopy (SEM) images of pure Ag_2WO_4 and the Ag_3PO_4/g-C_3N_4/Ag_2WO_4 composite. Fig. 4a shows a rod-like structure, and the average diameter of the nanorods was ~100 nm. The Ag_3PO_4/g-C_3N_4/Ag_2WO_4 composite displays a similar morphology to that of pure Ag_2WO_4 (Fig. 4b), showing that loading Ag_3PO_4 nanocrystals and g-C_3N_4 QDs did not have any significant influence on the morphology of the Ag_2WO_4 nanorods. The as-prepared Ag_3PO_4 sample was composed of nanocrystals with average sizes of ~20 nm (Fig. S1†). A TEM image of g-C_3N_4 QDs is shown in Fig. S2,† revealing that the prepared g-C_3N_4 QDs are monodispersed in the water solution and that each QD is uniform in size. Fig. 4c shows a TEM image of an individual Ag_3PO_4/g-C_3N_4/Ag_2WO_4 nanorod. It can be seen that Ag_3PO_4 nanocrystals and g-C_3N_4 QDs were loaded on the surface of the Ag_2WO_4 nanorod. A high-resolution TEM image of the Ag_3PO_4/g-C_3N_4/Ag_2WO_4 composite reveals that the crystal lattice fringe patterns are ~0.336 and ~0.213 nm (Fig. 4d), which correspond to the (002) crystal plane of g-C_3N_4 and the (210) crystal plane of Ag_3PO_4, respectively. The lattice distance of 0.229 nm in the nanorod is correlated to the (421) crystal plane of Ag_2WO_4 (Fig. 4e).

The BET surface areas of pure Ag_2WO_4 and Ag_3PO_4/g-C_3N_4/Ag_2WO_4 were analyzed using an automated surface area analyzer (Fig. 5). The calculated BET surface area of Ag_3PO_4/g-C_3N_4/Ag_2WO_4 is 110.602 $m^2\ g^{-1}$, which is larger than that of pure Ag_2WO_4 (20.817 $m^2\ g^{-1}$). It can be concluded that the loading of Ag_3PO_4 and g-C_3N_4 QDs can facilitate more efficient

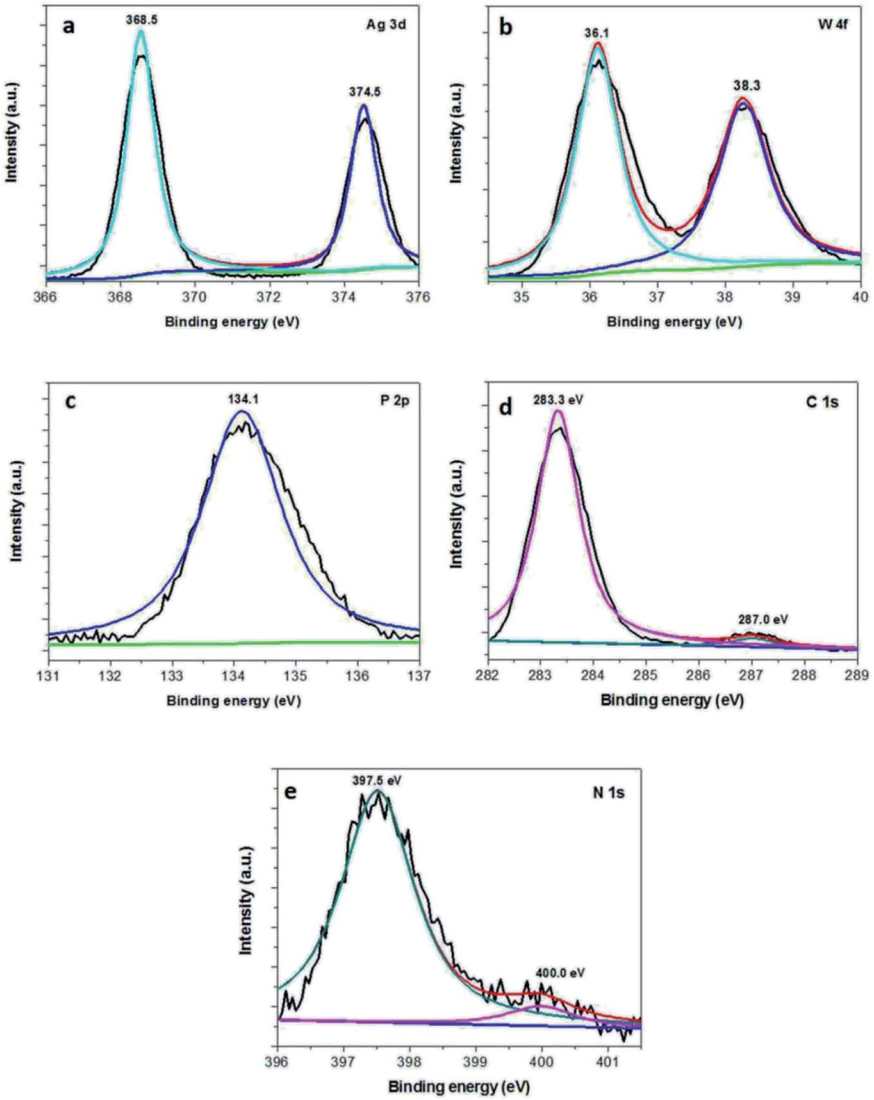

Fig. 3 XPS spectra of the as-obtained 30% Ag_3PO_4/g-C_3N_4/Ag_2WO_4: (a) Ag 3d, (b) W 4f, (c) P 3p, (d) C 1s, and (e) N 1s.

contact of the Ag_3PO_4/g-C_3N_4/Ag_2WO_4 composite with organic contaminants, which is beneficial to the improvement of photocatalytic performance.[19]

UV-vis DRS are shown in Fig. 6 to study the optical absorption properties of the Ag_3PO_4/g-C_3N_4/Ag_2WO_4 composite. The band gap of anatase Ag_2WO_4 is ~3.20 eV, so its absorption onset is located at 410 nm. The band gap for g-C_3N_4 QDs is 2.75 eV, corresponding to the absorption onset of 450 nm. In addition, the band gap of Ag_3PO_4 is calculated to be 2.13 eV, indicating an absorption onset at ~580 nm. In comparison with pure Ag_2WO_4, the Ag_3PO_4/g-C_3N_4/Ag_2WO_4 composite shows an absorption in the visible range that accompanies a red shift in the absorption edge resulting from the synergistic effect among Ag_2WO_4, Ag_3PO_4, and g-C_3N_4. The results reveal that the obtained Ag_3PO_4/g-C_3N_4/Ag_2WO_4 composite could be employed as a visible-light photocatalyst. The chronoamperometric *I–t* curves are shown in Fig. S3.† Compared with pure Ag_2WO_4, the Ag_3PO_4/g-C_3N_4/Ag_2WO_4 composite exhibited enhanced photocurrent responses. The ternary nanoheterojunctions can facilitate photoelectron–hole separation and thus retard photoelectron–hole recombination in the Ag_3PO_4/g-C_3N_4/Ag_2WO_4 composite.[28–30]

In this study, Ag_3PO_4/g-C_3N_4/Ag_2WO_4 along with sole Ag_2WO_4 and g-C_3N_4/Ag_2WO_4 composite was tested for photocatalytic Rh B degradation under visible-light irradiation (Fig. 7a). The blank experiment demonstrated that Rh B was stable under visible-light irradiation for 80 min. The pure Ag_2WO_4 composite exhibited generally low photocatalytic performances, with only 40.0% Rh B degradation, after 80 min visible-light irradiation. The low performance is probably due to the fast recombination of photoinduced charges in the single Ag_2WO_4. Compared with the pure Ag_2WO_4 sample, the g-C_3N_4/Ag_2WO_4 composite exhibited enhanced photocatalytic efficiency (50% Rh B degradation). The photocatalytic activity of Ag_3PO_4/g-C_3N_4/Ag_2WO_4 further improved the degradation of Rh B under visible light (λ > 420 nm), which can be ascribed to the

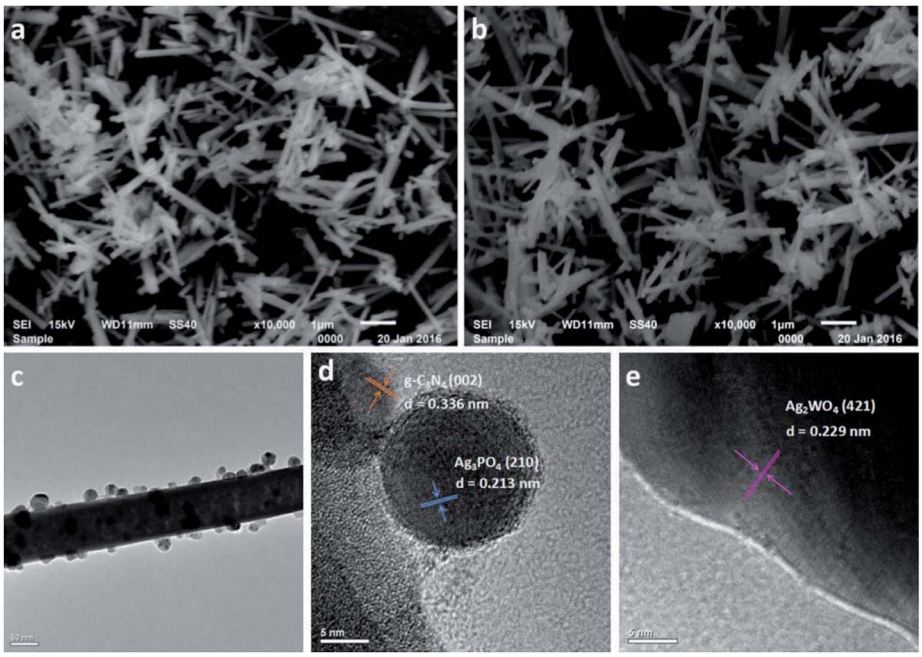

Fig. 4 SEM images of the as-prepared samples: (a) Ag_2WO_4 and (b) 30% Ag_3PO_4/g-C_3N_4/Ag_2WO_4. (c) TEM image of 30% Ag_3PO_4/g-C_3N_4/Ag_2WO_4. (d and e) High-resolution TEM images of 30% Ag_3PO_4/g-C_3N_4/Ag_2WO_4.

efficient separation of photogenerated electrons and holes through the ternary heterostructure. Among the Ag_3PO_4/g-C_3N_4/Ag_2WO_4 nanocomposites, the highest activity was obtained with the 30% Ag_3PO_4 loading sample, with which almost 100% of Rh B was photodegraded after 80 min of visible-light irradiation. This is because hybridization of Ag_2WO_4 with Ag_3PO_4 can result in efficient separation of photogenerated charges, thus improving the photocatalytic performance. However, too many Ag_3PO_4 can even cover the surface of Ag_2WO_4, which can reduce the density of active sites, thus reducing the photocatalytic efficiency. Therefore, the suitable loading content of Ag_3PO_4 is a primary prerequisite for optimizing the photocatalytic reaction.

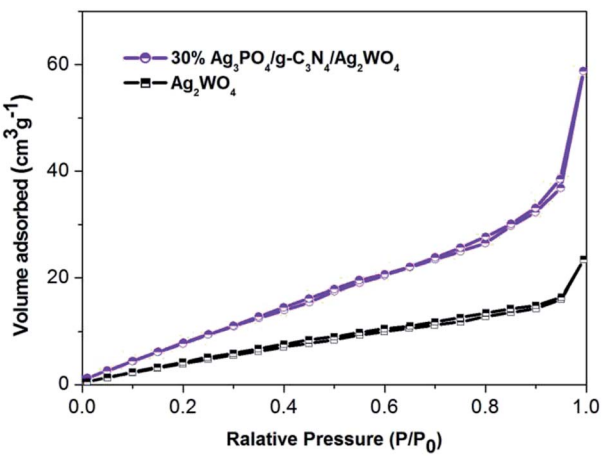

Fig. 5 N_2 adsorption–desorption isotherm curves of the as-prepared samples.

It is important to study the active species in the photocatalysis process. As shown in Fig. 7b, the photocatalytic efficiency of the 30% Ag_3PO_4/g-C_3N_4/Ag_2WO_4 composite was greatly suppressed after the addition of BQ and EDTA-2Na, indicating that $O_2^{\bullet-}$ and h^+ were the main reactive species. In addition, a slight decrease in the photocatalytic activity was observed by the addition of IPA, suggesting that ·OH was not the main reactive species.

The stability of the 30% Ag_3PO_4/g-C_3N_4/Ag_2WO_4 photocatalyst was studied through performing recycle experiments, as shown in Fig. 8. After four photocatalytic runs, the photocatalytic efficiency did not display any significant decay. The stability of the photocatalyst was also studied by using XRD (Fig. 9a) and SEM analysis (Fig. 9b) of fresh and used 30% Ag_3PO_4/g-C_3N_4/Ag_2WO_4. It can be seen that the phase structure, as well as the morphology of the 30% Ag_3PO_4/g-C_3N_4/Ag_2WO_4, remains intact after four recycles, revealing the high stability of the 30% Ag_3PO_4/g-C_3N_4/Ag_2WO_4 photocatalyst.

Based on the results and discussion above, heterostructure formed in the g-C_3N_4/Ag/$BiVO_4$ photocatalyst played an important role in the efficient separation of photoinduced charges. The potentials of VB and CB of a semiconductor can be calculated according to the following empirical equations:

$$E_{VB} = X - E^e + 0.5E_g \quad (1)$$

$$E_{CB} = E_{VB} - E_g \quad (2)$$

where E_{VB} is the valence band edge potential, E_{CB} is the conduction band edge potential, X is the electronegativity of the semiconductor, which is the geometric mean of the electronegativity of the constituent atoms, E^e is the energy of free

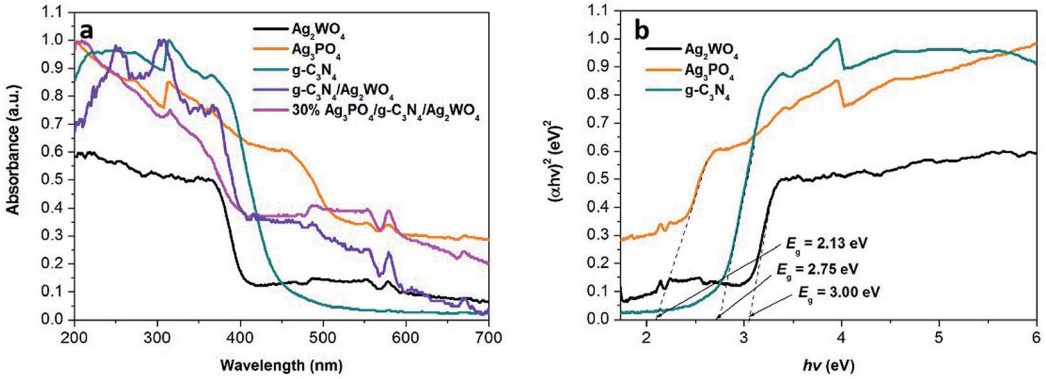

Fig. 6 UV-vis diffuse reflection spectra of the as-obtained samples. (b) Plots of $(\alpha h\nu)^2$ *versus* photon energy ($h\nu$) for the band gap energies of Ag_3PO_4, g-C_3N_4, and Ag_2WO_4.

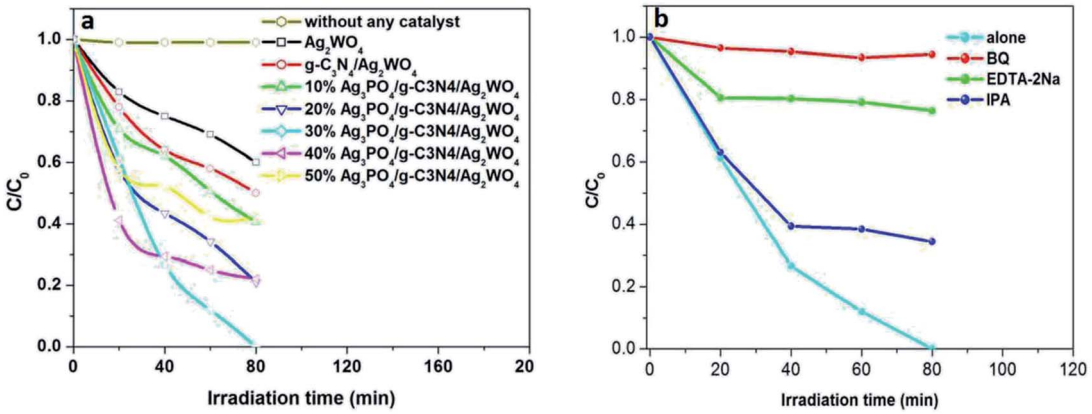

Fig. 7 (a) Photodegradation efficiencies of Rh B as a function of irradiation time for different photocatalysts. (b) Trapping experiment of active species during the photocatalytic degradation of Rh B over C_{60}CNTs/bismuth-based oxide nanocomposites under visible-light irradiation.

electrons on the hydrogen scale (about 4.5 eV), E_g is the band gap energy of the semiconductor. According to the DRS characterization results (Fig. 6) and eqn (1) and (2), the valence band (VB) edges of g-C_3N_4 QDs, Ag_2WO_4, and Ag_3PO_4 were measured to be +1.585, 2.73, and 2.535 eV *versus* SHE, respectively, while the conduction band (CB) edges for g-C_3N_4 QDs, Ag_2WO_4, and Ag_3PO_4 were −1.165, −0.27, and 0.505 eV *versus* SHE, respectively.

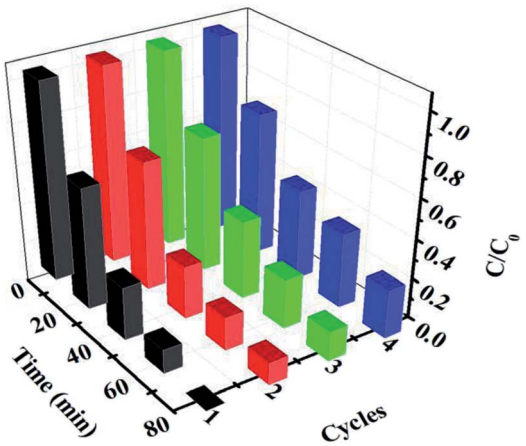

Fig. 8 Cycling runs for the photocatalytic degradation of Rh B over the ternary nanocomposites under visible-light irradiation.

Fig. 10 shows the proposed mechanism for the charge-carrier transfer process in the Ag_3PO_4/g-C_3N_4/Ag_2WO_4 photocatalyst. When the Ag_3PO_4/g-C_3N_4/Ag_2WO_4 composite is irradiated, electrons can be excited from CBs of g-C_3N_4 QDs and Ag_3PO_4. Because the CB position of g-C_3N_4 QDs was more negative than that of Ag_2WO_4 and Ag_3PO_4, the photogenerated electrons in the CB of g-C_3N_4 QDs can easily flow into the CB of Ag_2WO_4 or Ag_3PO_4, leading to the redistribution of electrons and holes so that the oxidation reaction is highly likely to take place and effectively prevent the electron–hole recombination process. Resulting in the improved photocatalytic performance of the Ag_3PO_4/g-C_3N_4/Ag_2WO_4 composite photocatalyst. The holes in the VB of Ag_3PO_4 with strong oxidation power can directly degrade Rh B. In addition, the electrons on the g-C_3N_4 can react with O_2 to produce $\cdot O^{2-}$, which can completely oxidize organic molecules to water and carbon dioxide.[31,32]

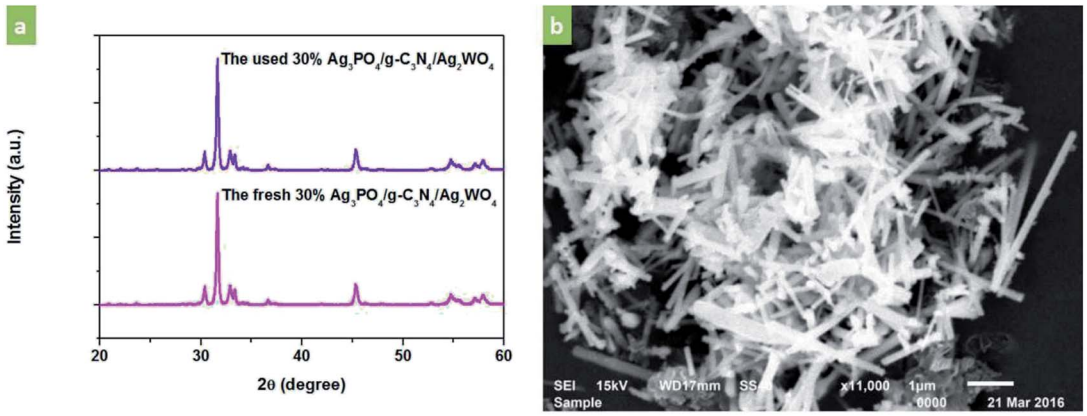

Fig. 9 (a) XRD patterns of the as-prepared 30% Ag_3PO_4/g-C_3N_4/Ag_2WO_4 sample before and after photocatalysis. (b) SEM image of the 30% Ag_3PO_4/g-C_3N_4/Ag_2WO_4 sample after photocatalysis.

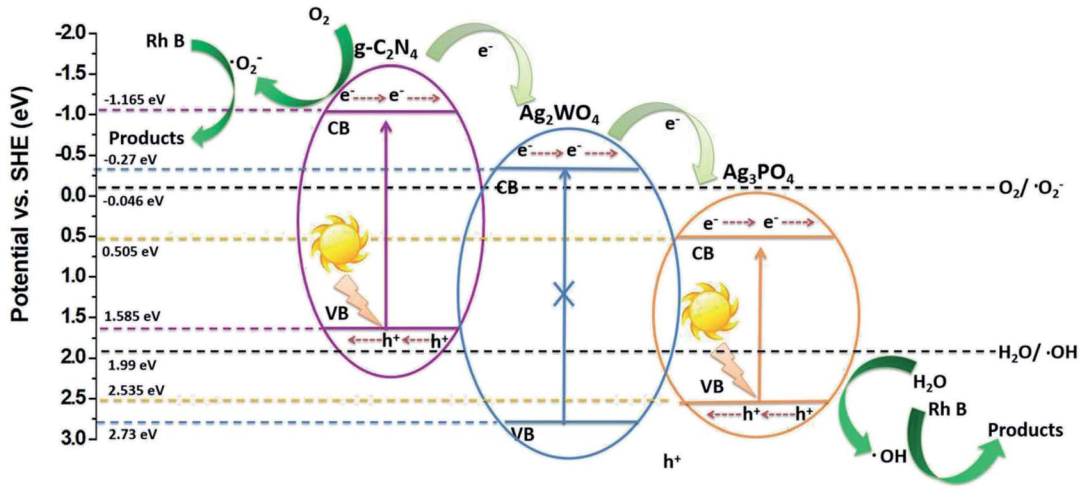

Fig. 10 Schematic diagram of the separation and transfer of photogenerated charges in the Ag_3PO_4/g-C_3N_4/Ag_2WO_4 composite photocatalyst under visible-light irradiation.

4. Conclusions

In summary, novel Ag_3PO_4/g-C_3N_4/Ag_2WO_4 nanorods were successfully synthesized by using simple deposition–precipitation of Ag_3PO_4 nanocrystals and g-C_3N_4 QDs on Ag_2WO_4 nanorods. The as-prepared Ag_3PO_4/g-C_3N_4/Ag_2WO_4 nanostructures showed excellent photocatalytic performance on the decolorization of Rh B, which was superior to those of pure Ag_2WO_4, or g-C_3N_4/Ag_2WO_4 under visible-light irradiation ($\lambda > 420$ nm). The Ag_3PO_4 and g-C_3N_4 loading contributed to enhanced visible-light harvesting and reduced recombination of photogenerated electron–hole pairs owing to the synergistic effect of the heterojunction structure of Ag_3PO_4/g-C_3N_4/Ag_2WO_4, thereby leading to enhanced photocatalytic performance.

Conflicts of interest

There are no conflicts to declare.

Acknowledgements

This work was supported by the National Natural Science Foundation of China (21407059, 51603086) and the Open Subject of the State Key Laboratory of Rare Earth Resource Utilization (RERU2017011).

References

1 D. Wang, Y. Duan, Q. Luo, X. Li and L. Bao, *Desalination*, 2011, **270**, 174–180.
2 H. G. Yu, L. Liu, X. F. Wang, P. Wang, J. G. Yu and Y. H. Wang, *Dalton Trans.*, 2012, **41**, 10405–10411.
3 H. J. Dong, G. Chen, J. X. Sun, C. M. Li, Y. G. Yu and D. H. Chen, *Appl. Catal., B*, 2013, **134**, 46–54.
4 C. Dong, K. L. Wu, X. W. Wei, X. Z. Li, L. Liu, T. H. Ding, J. Wang and Y. Ye, *CrystEngComm*, 2014, **16**, 730–736.

5 X. F. Wang, S. F. Li, H. G. Yu, J. G. Yu and S. W. Liu, *Chem.–Eur. J.*, 2011, **17**, 7777–7780.
6 Y. P. Bi, S. X. Ouyang, N. Umezawa, J. Y. Cao and J. H. Ye, *J. Am. Chem. Soc.*, 2011, **133**, 6490–6492.
7 H. P. Chen, N. Chen, C. P. Feng and Y. Gao, *J. Colloid Interface Sci.*, 2018, **515**, 119–128.
8 D. F. Xu, B. Cheng, S. W. Cao and J. G. Yu, *Appl. Catal., B*, 2015, **164**, 380–388.
9 S. Mandal and R. Ananthakrishnan, *ACS Sustainable Chem. Eng.*, 2018, **6**(1), 1091–1104.
10 Z. Y. Lin, J. L. Li, Z. Q. Zheng, J. H. Yan, P. Liu, C. X. Wang and G. W. Yang, *ACS Nano*, 2015, **9**, 7256–7265.
11 X. F. Wang, S. Zhan, Y. Wang, P. Wang, H. G. Yu, J. G. Yu and C. Z. Hu, *J. Colloid Interface Sci.*, 2014, **422**, 30–37.
12 X. H. Liu, J. L. Hu, J. J. Li, Y. Hu, Y. Shao, H. J. Yang, G. X. Tong and H. S. Qian, *Mater. Lett.*, 2013, **91**, 129–132.
13 V. M. Longo, C. C. D. Foggi, M. M. Ferrer, A. F. Gouveia, R. S. André, W. Avansi, C. E. Vergani, A. L. Machado, J. André, L. S. Cavalcante, A. C. Hernandes and E. Longo, *J. Phys. Chem. A*, 2014, **118**, 5769–5778.
14 L. Liu, Y. H. Qi, J. R. Lu, S. L. Lin, W. J. An, Y. H. Liang and W. Q. Cui, *Appl. Catal., B*, 2016, **183**, 133–141.
15 E. Grilla, A. Petala, Z. Frontistis, I. K. Konstantinou, D. I. Kondarides and D. Mantzavinos, *Appl. Catal., B*, 2018, **231**, 73–81.
16 L. Liu, L. Ding, Y. G. Liu, W. J. An, S. L. Lin, Y. H. Liang and W. Q. Cui, *Appl. Catal., B*, 2017, **201**, 92–104.
17 W. B. Li, C. Feng, S. Y. Dai, J. G. Yue, F. X. Hua and H. Hou, *Appl. Catal., B*, 2015, **168**, 465–471.
18 W. J. Shan, Y. Hu, Z. G. Bai, M. M. Zheng and C. H. Wei, *Appl. Catal., B*, 2016, **188**, 1–12.
19 J. Y. Su, L. Zhu and G. H. Chen, *Appl. Catal., B*, 2016, **186**, 127–135.
20 L. Xu, H. N. Li, J. X. Xia, L. G. Wang, H. Xu, H. Y. Ji, H. M. Li and K. Y. Sun, *Mater. Lett.*, 2014, **128**, 349–353.
21 Y. Wang, G. Q. Tan, T. Liu, Y. N. Su, H. J. Ren, X. L. Zhang, A. Xia, L. Lv and Y. Liu, *Appl. Catal., B*, 2018, **234**, 37–49.
22 X. L. Liu, P. Wang, H. S. Zhai, Q. Q. Zhang, B. B. Huang, Z. Y. Wang, Y. Y. Liu, Y. Dai, X. Y. Qin and X. Y. Zhang, *Appl. Catal., B*, 2018, **232**, 521–530.
23 D. F. Xu, B. Cheng, W. K. Wang, C. J. Jiang and J. G. Yu, *Appl. Catal., B*, 2018, **231**, 368–380.
24 W. J. Wang, J. C. Yu, Z. R. Shen, D. K. L. Chan and T. Gu, *Chem. Commun.*, 2014, **50**, 10148–10150.
25 Z. Y. Lin, J. L. Li, Z. Q. Zheng, J. H. Yan, P. Liu, C. X. Wang and G. W. Yang, *ACS Nano*, 2015, **9**, 7256–7265.
26 X. P. Wang, L. X. Wang, F. Zhao, C. G. Hu, Y. Zhao, Z. P. Zhang, S. L. Chen, G. Q. Shi and L. T. Qu, *Nanoscale*, 2015, **7**, 3035–3042.
27 L. Liu, Y. H. Qi, J. R. Lu, S. L. Lin, W. J. An, Y. H. Liang and W. Q. Cui, *Appl. Catal., B*, 2016, **183**, 133–141.
28 S. H. Zhan, Q. L. Hou, Y. Li, S. L. Ma, P. F. Wang, Y. N. Li and H. T. Wang, *RSC Adv.*, 2018, **8**, 34428–34436.
29 C. Wang, G. L. Wang, X. F. Zhang, X. L. Dong, C. Ma, X. X. Zhang, H. C. Ma and M. Xue, *RSC Adv.*, 2018, **8**, 18419–18426.
30 Y. J. Zou, J. W. Shi, D. D. Ma, Z. Y. Fan, C. M. Niu and L. Z. Wang, *Chemcatchem*, 2017, **9**, 3752–3761.
31 B. C. Zhu, P. F. Xia, Y. Li, W. K. Ho and J. G. Yu, *Appl. Surf. Sci.*, 2017, **391**, 175–183.
32 W. Liu, J. Shen, X. F. Yang, Q. Q. Liu and H. Tang, *Appl. Surf. Sci.*, 2018, **456**, 369–378.